A turbulence model study of separated 3D jet/afterbody flow

R. G. M. Hasan and J. J. McGuirk
Loughborough University
Loughborough, UK

D. D. Apsley
Department of Civil Engineering, UMIST
Manchester, UK

M. A. Leschziner
Department of Aeronautics
Imperial College of Science, Technology and Medicine
London, UK

ABSTRACT

Three-dimensional RANS calculations and comparisons with experimental data are presented for subsonic and transonic flow past a non-axisymmetric (rectangular) nozzle/afterbody typical of those found in fast-jet aircraft. The full details of the geometry have been modelled, and the flow domain includes the internal nozzle flow and the jet exhaust plume. The calculations relate to two free-stream Mach numbers of 0·6 and 0·94 and have been performed during the course of a collaborative research programme involving a number of UK universities and industrial organisations. The close interaction between partners contributed greatly to the elimination of computational inconsistencies and to rational decisions on common grids and boundary conditions, based on a range of preliminary computations. The turbulence models used in the study include linear and non-linear eddy-viscosity models. For the lower Mach number case, the flow remains attached and all of the turbulence models yield satisfactory pressure predictions. However, for the higher Mach number, the flow over the afterbody is massively separated, and the effect of turbulence model performance is pronounced. It is observed that non-linear eddy-viscosity modelling provides improved shock capturing and demonstrates significant turbulence anisotropy. Among the linear eddy-viscosity models, the SST model predicts the best surface pressure distributions. The standard $k-\varepsilon$ model gives reasonable results, but returns a shock location which is too far downstream and displays a delayed recovery. The flow field inside the jet nozzle is not influenced by turbulence modelling, highlighting the essentially inviscid nature of the flow in this region. However, the resolution of internal shock cells for identical grids is found to be dependent on the solution algorithm – specifically, whether it solves for pressure or density as a main dependent variable. Density-based time-marching schemes are found to return a better resolution of shock reflection. The paper also highlights the urgent need for more detailed experimental data in this type of flow.

NOMENCLATURE

$\boldsymbol{a}$	anisotropy tensor
a_1	coefficient in SST model shear stress limiter
a_{ij}	anisotropy tensor
C_p	static pressure coefficient
C_μ , C_μ^*	empirical constant or function
$C_{\varepsilon 1}$, $C_{\varepsilon 2}$	empirical constants
f_μ	viscous damping function
F_1, F_2	blending functions
$\boldsymbol{I}$	identity tensor
k	kinetic energy of turbulence
L	axial length of afterbody/nozzle geometry
M	Mach number

Paper No. 2760. Manuscript received 24 June 2002, accepted 20 February 2003.

https://doi.org/10.1017/S0001924000004942 Published online by Cambridge University Press

p	static pressure
P_{tj}	jet total pressure
P_p	Pitot pressure
$P_{to`}$	jet outlet total pressure
R	radius (non-dimensional)
$\boldsymbol{s}$	strain tensor
$s_2 (= S_{ij} S_{ij})$	dimensionless strain invariant
S_{ij}	strain rate tensor (dimensionless)
t	time
T_{ij}^k	upper partition tensor
$\mathbf{U_i}$, $\mathbf{U_j}$, $\mathbf{U_k}$	mean velocity vector
U_{max}	maximum backflow velocity
U, V, W	mean velocities in streamwise and radial directions
$\boldsymbol{w}$	vorticity tensor
$w_2 (= \Omega_{ij} \Omega_{ij})$	dimensionless vorticity invariant
$\overline{uu}, \overline{vv}, \overline{ww},$	Reynolds normal stresses
$\overline{uv}$	Reynolds shear stress
$\overline{u_i u_j}$	Reynolds stresses
x_i, x_j, x_k	position vector
x, y, z	cartesian co-ordinates
X, Y, Z	distances (non-dimensional) in streamwise and radial directions

Greek symbols

ak	constants
$\beta_1, \beta_2, \beta_3$	constants
δ_{ij}	Kronecker delta
δ	size of backflow region
$\gamma_1, \gamma_2, \gamma_3, \gamma_4$	coefficients
Ω	mean vorticity
Ω_{ij}	vorticity tensor (dimensionless)
ε	dissipation rate of turbulence
μ, μ_t	molecular/turbulent viscosity
ρ	density of fluid
$\varphi, \varphi_1, \varphi_2$	coefficients
$\sigma_k, \sigma_\varepsilon, \sigma_\omega$	coefficients
τ	time scale
ω	specific dissipation rate

1.0 INTRODUCTION

The afterbody of a supersonic military aircraft can contribute up to 50% of the aircraft's total drag. In general, this drag arises as a combination of four elements:

(*i*) wave drag associated with a shock on the afterbody, formed as a consequence of the supersonic boattail flow being deflected by the jet exhaust plume;

(*ii*) flow separation from the afterbody surface, provoked by the shock interacting with the afterbody boundary layer;

(*iii*) the curvature of the boattail boundary layer, which causes suction on the boattail surface; and

(*iv*) frictional drag – usually a subordinate contribution, unless the boundary layer is strongly three-dimensional and the afterbody includes large fins and stabilising surfaces.

The above operationally-important processes, and the fact that the flow on the boattail can have a substantial effect on the aerodynamic, thermal and acoustic characteristics of the jet emanating from the exhaust nozzle, provide strong motivation for understanding the basic physical mechanisms involved and for developing computational procedures that accurately describe jet/afterbody flows. The substantial interest in this area is reflected by two major AGARD compendia[1,2] which provide surveys of the state of the art in afterbody aerodynamics in 1986 and 1995, respectively.

Jet/afterbody flows involve a number of physically complex processes which must be appreciated in relation to their computational modelling. The boundary layer approaching the boattail is generally thick and highly turbulent. As it progresses along the curved boattail, it accelerates, becoming supersonic (unless already in that state) if the free-stream Mach number upstream of the boattail exceeds approximately 0·7. The deflection of this supersonic flow by the downstream-located jet exhaust plume provokes a shock which interacts with the boattail boundary layer just upstream of the jet nozzle exit, causing it to decelerate and thicken rapidly. If this shock is sufficiently strong, the boundary layer separates from the boattail surface, and a recirculation bubble is formed above the boattail, possibly extending beyond the afterbody into the jet region. The jet itself is usually under-expanded and thus features a complex structure of shock cells and Mach disks (depending on nozzle pressure ratio) in which the flow undergoes repeated compressions and expansions. If the jet issues from a convergent-divergent nozzle, it is already supersonic at the nozzle exit, and its structure at exit may be affected by shock reflections within the divergent part of the nozzle. The jet's outer shear layer is highly turbulent and perturbed, both in terms of its mean-flow structure and turbulence state, by the shocks interacting with the internal nozzle boundary layer and the repeated external shock reflections associated with the expansion process of the jet. The jet spreading in its turn is strongly affected by the boattail boundary layer, which merges into the jet, this interaction being especially complex if the flow on the boattail is separated.

The physical phenomena identified above pose major computational and modelling challenges. There is, first, the need to maintain sufficient numerical accuracy to resolve the multiple-shock pattern and also the rapidly-evolving shear layers on the afterbody and in the jet. If the afterbody itself is the primary focus of attention, a key requirement is the ability of the numerical scheme to capture the afterbody shock, its interaction with the turbulent afterbody boundary layer and the details of the separated region provoked by the interaction. To this end, the scheme must be at least second-order accurate, limit artificial dissipation to a minimum and be supported by a sufficiently fine grid, especially in the important shock/boundary-layer and jet/afterbody-wake interaction regions.

In considering the approach to modelling turbulence, it must be recognised first that, unlike 2D thin shear flows in which only one shear stress is dynamically active, jet/afterbody flows feature strong normal straining and are also affected by curvature. While straining arising from the latter may be relatively weak, its influence may nevertheless be significant, because turbulence is highly sensitive to streamline curvature. In three dimensions, strong streamwise vorticity may be generated, in which case, several (if not all) turbulent-stress components may be dynamically active. The presence of strong normal straining, both in the shock-affected boattail boundary layer and in the jet, and the possible existence of a separation region above the boattail, imply the need for a turbulence model that distinguishes the radically different effects arising from shear and normal straining, and which predicts not only the shear stress correctly, but also returns a realistic representation of the normal stresses. This ability is also pertinent to the representation of the sensitive interaction between turbulence and curvature-related straining, both in the boattail boundary layer and the recirculation region. Here again, this interaction is closely linked to anisotropy of the normal stresses and its linkage to the shear stress. Finally, attention is required to the resolution of the semi-viscous near-wall region. As the shock wave provokes strong streamwise changes in the boundary layer, its structure is complex and far from the state of equilibrium that is often described by the universal law of the wall. As the separation point or line is sensitive to the turbulence structure close to the wall, it follows that a turbulence model expected to give a realistic representation of separation must be able to account for the effects of viscosity on the turbulence structure. Such a model must therefore be applicable to low-Reynolds-number flows.

The present paper investigates the ability of two computational approaches and several turbulence models to predict the flow around the rectangular jet/afterbody geometry shown in Fig. 1.

https://doi.org/10.1017/S0001924000004942 Published online by Cambridge University Press

Measurements of this flow were performed by Putnam and Mercer[3] for two free-stream Mach numbers, 0·60 and 0·94. This geometry, whilst evidently three-dimensional, gives rise to features which are qualitatively similar to those observed in axisymmetric cases which have been investigated much more intensively. It therefore allows key observations derived from the present computations to be rationally linked to past experience. The results reported here have arisen from a broad university-industry collaborative project (VoTMATA - Validation of Turbulence Models for Aerospace and Turbomachine Applications) which involved Loughborough University, UMIST, BAE Systems, QinetiQ (formerly DERA), ARA and Rolls-Royce. This project set out to identify the capabilities and range of applicability of several types of turbulence models, including advanced non-linear eddy-viscosity models and second-moment closure, on the basis of computations for a number of flow configurations which are pertinent to aerospace applications. Aspects of this collaboration and the outcome of studies dealing, respectively, with a separated diffuser flow, the flow around a wing-body junction and the flow around a transonic bump on a cylinder, are documented in references[4,5,6]. The last-mentioned test case may be viewed as a precursor to the current study, since it represents the flow around an axisymmetric afterbody shape, with the emerging 'jet' represented by the downstream portion of the solid cylinder. A key feature of the collaboration was the use of identical numerical meshes and a collective and close scrutiny of differences arising from the various computational approaches. This interactive approach increases the degree of confidence in the validity of the conclusions derived from the project.

The directions of previous studies on afterbody flows have been dictated mainly by the availability of experimental data. With very few exceptions (e.g. AGARD A1 and ONERA A2 afterbodies[1]. such data are confined to afterbody surface pressure. In addition, the majority apply only to two-dimensional jet/afterbody or sting/afterbody configurations (e.g. Carson and Lee[7], Reubush[8,9], Bachalo and Johnson[10], NASA Langley, AGARD and ONERA afterbodies[1,2]). The majority of computational studies reported prior to 1995 were undertaken with linear eddy-viscosity models, some as simple as the Baldwin-Lomax model[11] and its combination with the Goldberg backflow model[12]. Studies by Peace[13], Newbold[14], Carlson *et al*[15] and Compton[16] with the $k-\varepsilon$ model applied to the AGARD and ONERA jet/afterbody flows represent the state of the art, in terms of modelling sophistication, around 1995/6. Later studies by Carlson[17], Loyau *et al*[18], Batten *et al*.[19,20], Barakos and Drikakis[21] and Hasan and McGuirk[5] investigated the performance of more elaborate non-linear eddy-viscosity and Reynolds-stress-transport models, in comparison to simpler linear eddy-viscosity formulations, using in part test cases reviewed by Berrier[22]. All of these studies gave priority to prediction of two-dimensional configurations. The principal conclusion emerging from these more recent studies is that anisotropy-resolving non-linear eddy-viscosity and Reynolds-stress models tend to return a substantially greater sensitivity to the shock, representing more accurately than standard linear eddy-viscosity models the process of shock-induced separation and the surface-pressure plateau associated with the separated region above the boattail. Menter's two-equation ($k-\varepsilon/k-\omega$) model[23] is one linear eddy-viscosity form found to give a performance which, in some respects, was similar to that of the more elaborate models, however, this variant relies on a specific and highly influential limitation of the shear stress in the boundary layer, and the generality of this aspect of the model is perhaps doubtful.

Previous computational investigations have also been performed specifically for the 3D configuration examined herein. Early studies were undertaken at NASA by Abdol-Hamid and Compton around 1990[16, 24, 25], mostly with the algebraic Baldwin-Lomax model. It is now generally accepted, however, that this model is inappropriate for separated flows and the level of agreement with measurements in this early work was as a consequence poor. More recently, Leschziner *et al*[20] investigated two Reynolds-stress-transport models in comparison to two-equation linear eddy-viscosity models, deriving conclusions compatible with those emerging from studies on two-dimensional geometries. Their work concentrated mainly on assessment of the compressibility-adapted form of the turbulence model, and its performance in axisymmetric afterbody flows with solid plume simulators, or focussed attentions principally on the jet-base region. The application to 3D afterbodies only examined surface pressure predictions. The present study reports significant new information on the predictive characteristics of linear and non-linear eddy-viscosity models, as well as comparing the performance of density- and pressure-based solution schemes.

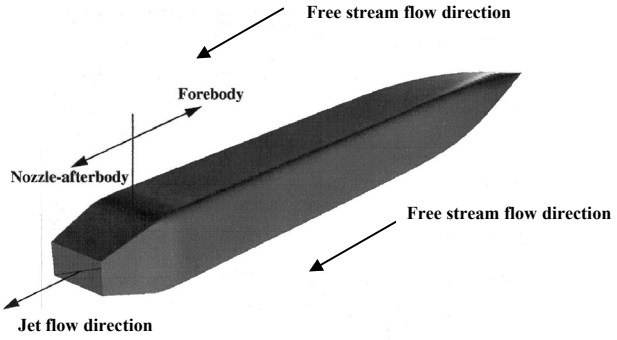


Figure 1. Model illustrating the afterbody (axial length, *L*).

2.0 TURBULENCE MODELS

Two categories of turbulence models have been investigated in the present study. One is based on the widely used linear stress-strain, eddy-viscosity relation:

$$a_{ij} \equiv \left(\frac{\overline{u_i u_j}}{k} - \frac{2}{3}\delta_{ij} \right) = -2C_\mu f_\mu S_{ij} \qquad \ldots (1)$$

where,

$$S_{ij} = \frac{\tau}{2}\left(\frac{\partial U_i}{\partial x_j} + \frac{\partial U_j}{\partial x_i} \right) - \frac{\tau}{3}\frac{\partial U_k}{\partial x_k}\delta_{ij} \qquad \ldots (2)$$

is the strain rate non-dimensionalised by the turbulent time scale τ (typically, k/ε in $k-\varepsilon$ models, or $1/\omega$ in $k-\omega$ models), C_μ is normally 0·09 and f_μ is a model-specific viscous-damping function . Models for which results are presented below are the standard high-Re $k-\varepsilon$ model of Jones and Launder[26], the standard $k-\omega$ model of Wilcox[27] and the Shear Stress Transport (SST) model of Menter[23].

The other model type adopts a non-linear relationship of the form:

$$a_{ij} = -2C_\mu^* f_\mu S_{ij} + \sum_k \alpha_k T_{ij}^k \left(S_{ij}, \Omega_{ij} \right) \qquad \ldots (3)$$

where T_{ij}^k are second-order tensor functions of the strain and vorticity tensors. While there are some 15 different models of this type, all may be written in the above canonical form, and in all the coefficients α_k are functions of the turbulence energy (a velocity scale), k, the turbulence time scale, τ, and (in most cases) also the second invariants of the vorticity and strain tensors. The coefficient C_μ^* corresponds to C_μ , but may contain a functional dependence on the strain and vorticity invariants.

The particular form considered in this study is a model of Craft *et al*[28] which uses the cubic relationship:

https://doi.org/10.1017/S0001924000004942 Published online by Cambridge University Press

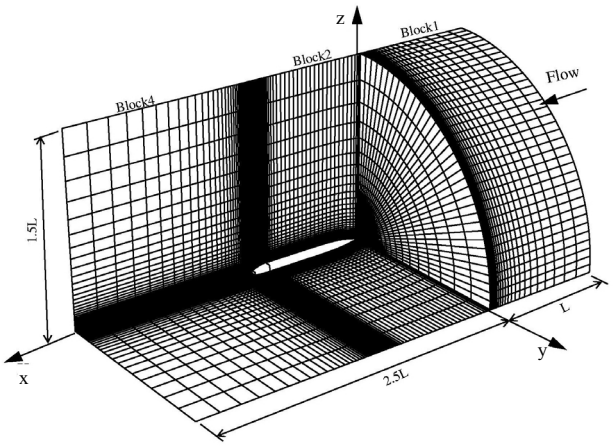


Figure 2(a). Computational domain and co-ordinate system.

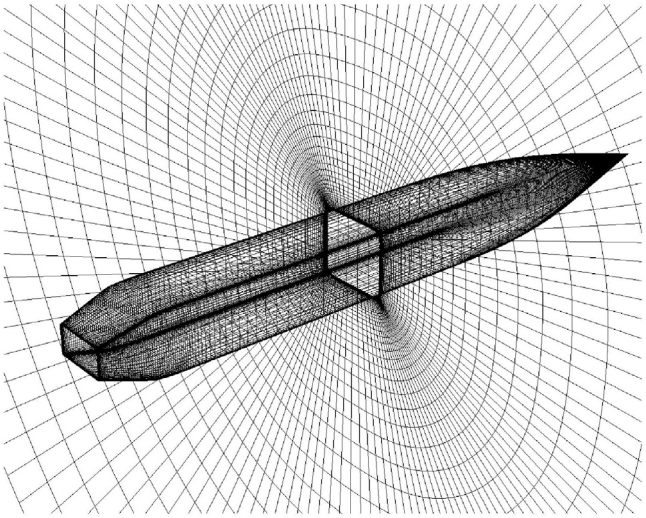


Figure 2(b). Overall grid distribution.

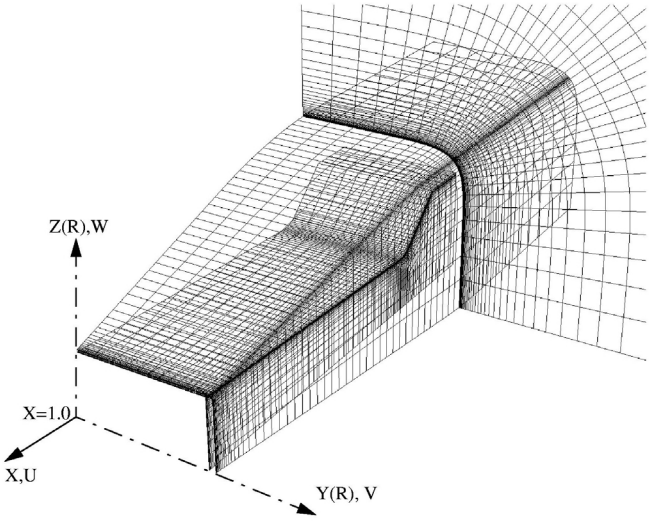


Figure 2(c). Close up of grid showing internal nozzle.

$$\boldsymbol{a} = -2\,C_\mu\,\boldsymbol{s} + \beta_1\,(\boldsymbol{s}^2 - 1/3\,s_2\,\boldsymbol{I}) + \beta_2\,(\boldsymbol{ws} - \boldsymbol{sw}) + \beta_3\,(\boldsymbol{w}^2 - 1/3\,w_2\,\boldsymbol{I}) - \gamma_1\,s_2\,\boldsymbol{s} - \gamma_2\,w_2\,\boldsymbol{s} - \gamma_3\,(\boldsymbol{w}^2\,\boldsymbol{s} + \boldsymbol{s}\,\boldsymbol{w}^2 - w_2\,\mathbf{s} - 2/3\{\boldsymbol{wsw}\}\boldsymbol{I}) - \gamma_4\,(\boldsymbol{w}\,\boldsymbol{s}^2 - \boldsymbol{s}^2\,\boldsymbol{w}) \quad \ldots (4)$$

where,

$$\boldsymbol{a} \equiv a_{ij};\ \ \boldsymbol{s} \equiv S_{ij};\ \ \boldsymbol{w} \equiv \Omega_{ij};\ \ \{\boldsymbol{wsw}\} \equiv \text{trace}\{\boldsymbol{wsw}\};\ \ \mathrm{I} \equiv \delta_{ij}$$

$$s_2 \equiv S_{ij}S_{ij};\quad w_2 \equiv \Omega_{ij}\Omega_{ij} \quad \ldots (5)$$

In all models considered, k is determined from the equation

$$\frac{\partial}{\partial t}(\rho k) + \frac{\partial}{\partial x_j}(\rho U_j k) = \frac{\partial}{\partial x_j}\left[\left(\mu + \frac{\mu_t}{\sigma_k}\right)\frac{\partial k}{\partial x_j}\right] - \rho\overline{u_i u_j}\frac{\partial U_i}{\partial x_j} - \rho\frac{k}{\tau} \quad \ldots (6)$$

The time scale, τ, is determined either via an equation for the dissipation rate, ε,

$$\frac{\partial}{\partial t}(\rho\varepsilon) + \frac{\partial}{\partial x_j}(\rho U_j \varepsilon) = \frac{\partial}{\partial x_j}\left[\left(\mu + \frac{\mu_t}{\sigma_\varepsilon}\right)\frac{\partial \varepsilon}{\partial x_j}\right] - \rho\frac{C_{\varepsilon 1}}{\tau}\overline{u_i u_j}\frac{\partial U_i}{\partial x_j} - C_{\varepsilon 2}\rho\frac{\varepsilon}{\tau} \quad \ldots (7)$$

or – as is the case of the models by Wilcox[27] and Menter[23] – from an equation for the specific dissipation, ω,

$$\frac{\partial}{\partial t}(\rho\omega) + \frac{\partial}{\partial x_j}(\rho U_j \omega) = \frac{\partial}{\partial x_j}\left[\left(\mu + \frac{\mu_t}{\sigma_\omega}\right)\frac{\partial \omega}{\partial x_j}\right] - \rho C_{\omega 1}\frac{1}{\tau}\overline{u_i u_j}\frac{\partial U_i}{\partial x_j} - C_{\omega 2}\rho\omega^2 \quad \ldots (8)$$

In the above equations, the turbulent viscosity is given by $\mu_t = \rho C_\mu k\tau$ and the constants or coefficients (including those in equation (4)) may be found in the relevant references given.

Menter's SST model[23] is constructed as a blend of the $k-\omega$ and the $k-\varepsilon$ models, the latter transformed in terms of k and ω. Blending is effected, in principle, by way of the interpolation:

$$\phi = F_1\phi_1 + (1 - F_1)\phi_2 \quad \ldots (9)$$

where ϕ_1 and ϕ_2 are any pair of analogous coefficients in the $k-\omega$ and $k-\varepsilon$ models, respectively. The function F_1 is designed such that it assumes the value of unity near the wall (thus activating the $k-\omega$ model) and zero away from the wall (implementing the $k-\varepsilon$ model). A second key element of the model is that the eddy-viscosity is modified (limited) so as to suppress the growth of the shear stress in high strain rates (e.g. strong adverse pressure gradient). The rationale lies in Bradshaw's assumption of a linear relationship between the shear stress and the turbulence energy in boundary layers. The limiter is implemented via the eddy-viscosity:

$$\mu_t = \frac{a_1\rho k}{\max(a_1\omega,\ \Omega F_2)} \quad \ldots (10)$$

where a_1 is a constant, Ω is the mean vorticity (corresponding to the strain rate) and F_2 is a function which is unity for boundary-layer flows and zero for free shear flows. This ensures that Bradshaw's assumption is satisfied in the boundary layer, while the original

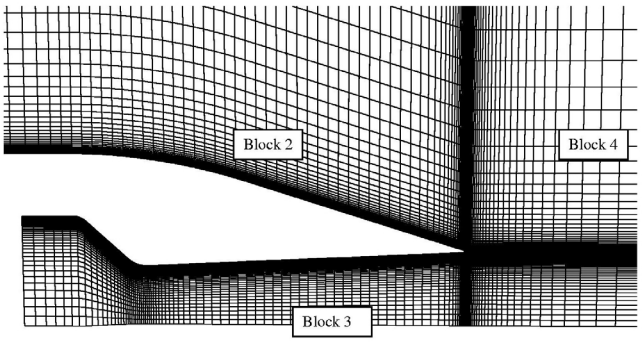


Figure 2(d). Details of mesh in vertical symmetry plane.

https://doi.org/10.1017/S0001924000004942 Published online by Cambridge University Press

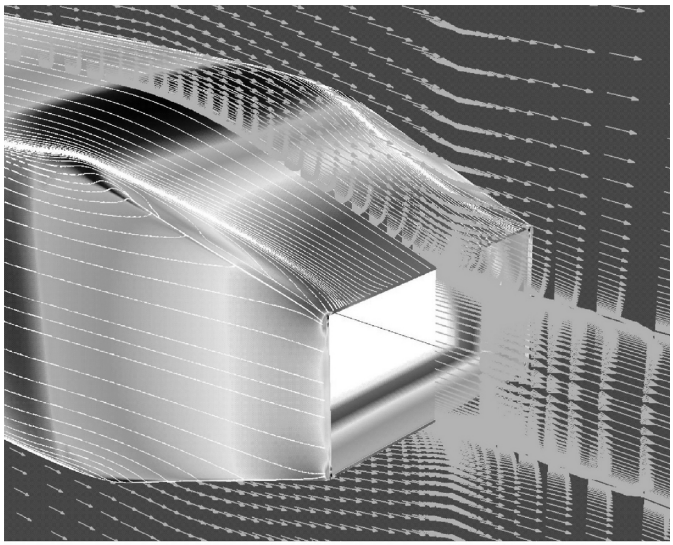
$k - \omega$ formulation is recovered for the remainder of the flow. The values of coefficients and the blending functions may be found in Menter[23].

3.0 EXPERIMENTAL SET-UP AND DATA

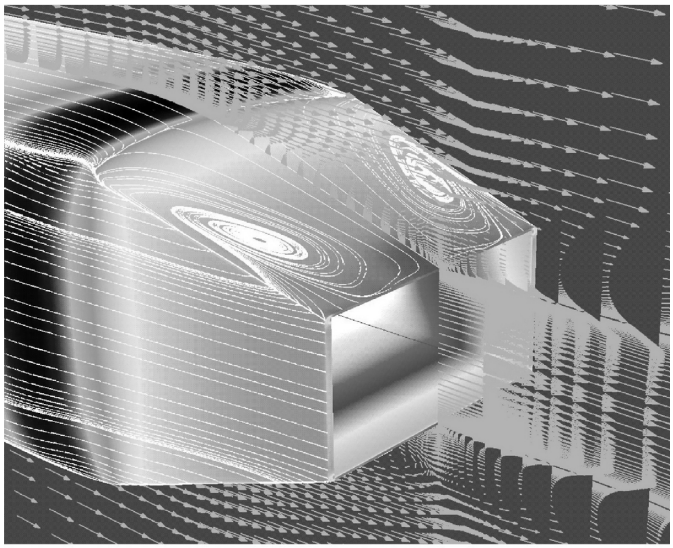
The experimental data, against which the current predictions are to be compared, were obtained in the NASA Langley 16ft transonic wind tunnel and are part of a broad database for nonaxisymmetric nozzles. The data are partly published in Putnam[3], and then more data were supplied to the AGARD working group[2]. A consolidated form of the data are also made available in Compton[16].

The tunnel was a continuous-flow, atmospheric, single-return facility with an octagonal slotted test section. High-pressure air was used to simulate the jet exhaust. Figure 2 gives a grid representation of the afterbody which is 63·04in (= 1·601m) long and consists of an isolated super-elliptic body (with no wing or tails) with a non-axisymmetric convergent-divergent nozzle attached. The model has a conical nose which blends smoothly into a super-elliptic cross-section. At the rear end, the afterbody is nearly rectangular in cross-section, with rounded corners. The top/bottom boattail angle is 17·56° and the side boattail angle is 6·93°. The detailed geometrical definition of the nozzle is available in analytic form and can be found in references[3,16]. Internally, the sidewalls of the nozzle are flat and parallel. The aspect ratio of the nozzle throat (i.e. the ratio of width to height) is 2·38, and the aspect ratio at the nozzle exit is 1·9. The ratio of exit-to-throat area is 1·25, which gives a design nozzle-pressure ratio of 4·25 and a design exit Mach number of 1·6. The centre-line of the model was aligned with the centre-line of the wind tunnel. The model blockage was 0·14%, and the maximum combined blockage of the model and support system was 0·19%.

Measurements were taken of surface pressures over the afterbody along five streamwise lines, and static pressure ratios along two streamwise lines in the internal nozzle. Two free-stream Mach numbers (0·60 and 0·94) were examined corresponding to a nominal Reynolds number of 20×10^6, defined with respect to the model length, L. For the lower Mach number, extensive pitot-pressure measurements were also made in the plume at three streamwise planes of x/L = 1·0, 1·08 and 1·16. No velocity or turbulence data over the body itself were reported for either test case.



(a) M = 0·60.



(b) M = 0·94.

Figure 3. Overall flow field on the afterbody (SST model), showing separation for M = 0·94.

4.0 NUMERICAL ISSUES

4.1 Solution domain and grids

Figure 2(a) shows the details of the computational domain, the grid and the co-ordinate system. Dimensional co-ordinates are indicated by lower-case letters, whereas dimensionless distances (scaled with the model length L) are in upper case. Figure 2(b) illustrates the overall grid distribution, and Fig. 2(c) and 2(d) gives a close-up view in the afterbody and nozzle section. For computational efficiency, symmetry was assumed with respect to both the vertical and horizontal planes, and only a quarter of the flow domain was considered. The domain extends 1L upstream from the model nose, 1·5L downstream from the nozzle exit and approximately 1·5L laterally from the model surface to the far-field boundary. Preliminary test computations verified that the boundary was sufficiently far from the model.

The overall domain (Fig. 2(a)) consists of 4 blocks: block 1 covers the section upstream of the afterbody nose, block 2 is the portion on the external afterbody, block 3 is the internal nozzle and block 4 contains the plume section. The grids are body-fitted with one-to-one connectivity between the blocks. The hexahedral grids were generated by an in-house algebraic method. Grid lines are clustered near the body surface, on the afterbody, near the nozzle exit, and at the nozzle throat. They are also clustered in the circumferential direction near the corners of the afterbody. Figure 2(d) shows details of the mesh in the vertical plane of symmetry of the nozzle. As mentioned before, no simplifications were made in respect of the geometry of the afterbody, and hence the small base (wall thickness) (~1mm) at the nozzle exit is meshed with 24 grid points (see Fig. 2(c)). Normal distances from the centres of the first cell to the wall are 0·0024mm and 0·0475mm for the low-Re and high-Re grids, respectively. In terms of the non-dimensional distance y^+, these values corresponded to approximately 1 and 40-100, respectively. The total number of cells used for the low-Re calculations is about 937,000.

4.2 Boundary conditions

Riemann invariants for one-dimensional flow were used to calculate the primitive flow variables ρ, U, V, W and p at the inflow boundary. At the outflow boundary, where the flow is a mixture of the jet exhaust and the free stream, all streamwise gradients were set to

https://doi.org/10.1017/S0001924000004942 Published online by Cambridge University Press

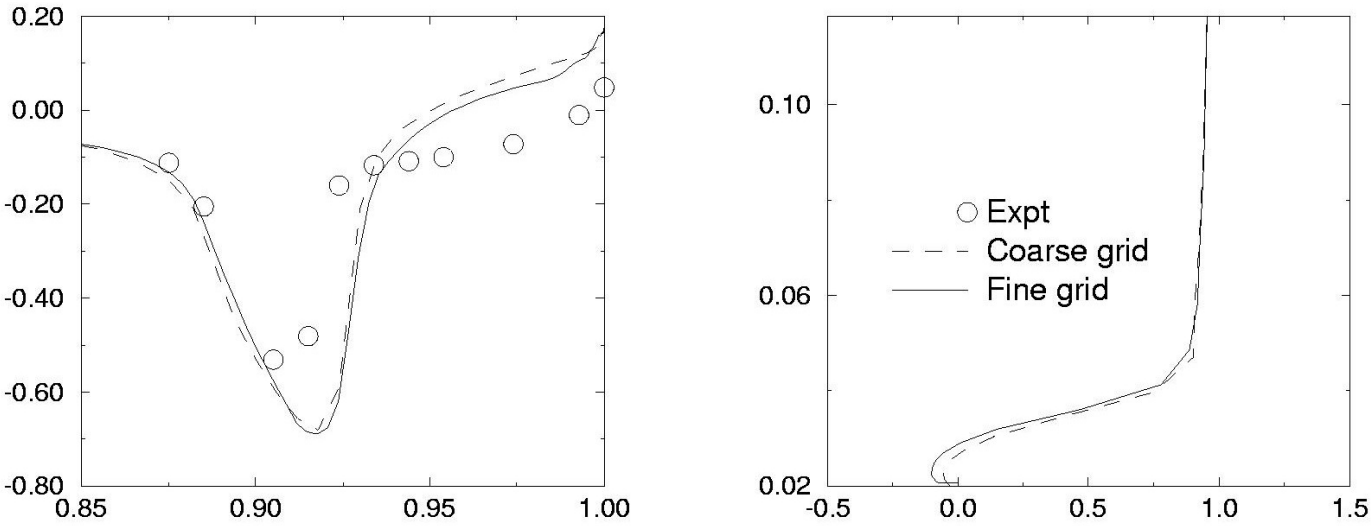
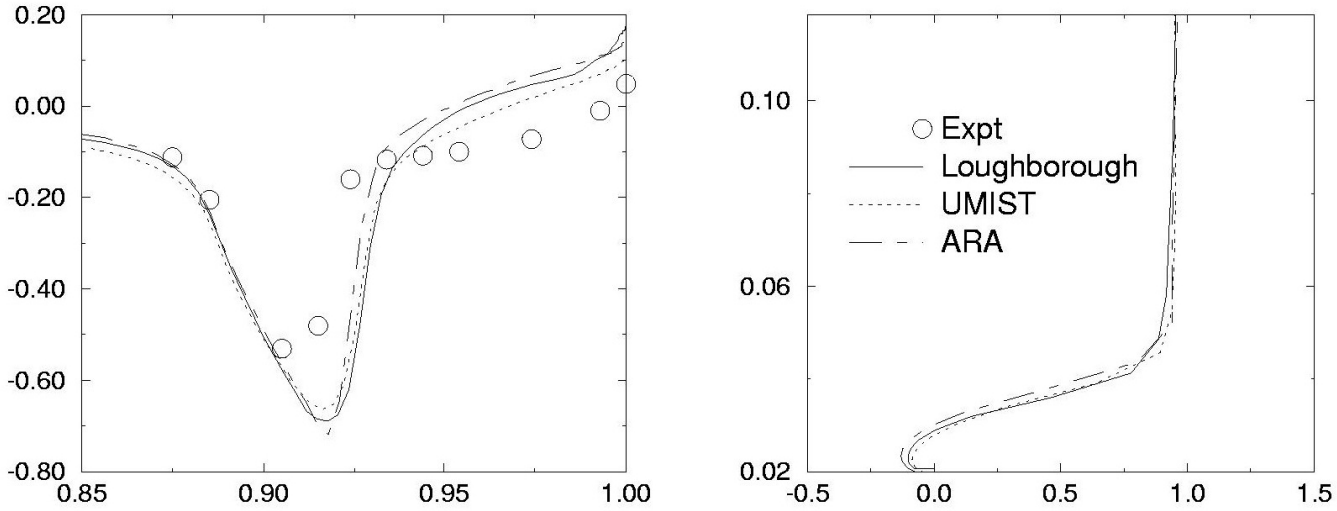
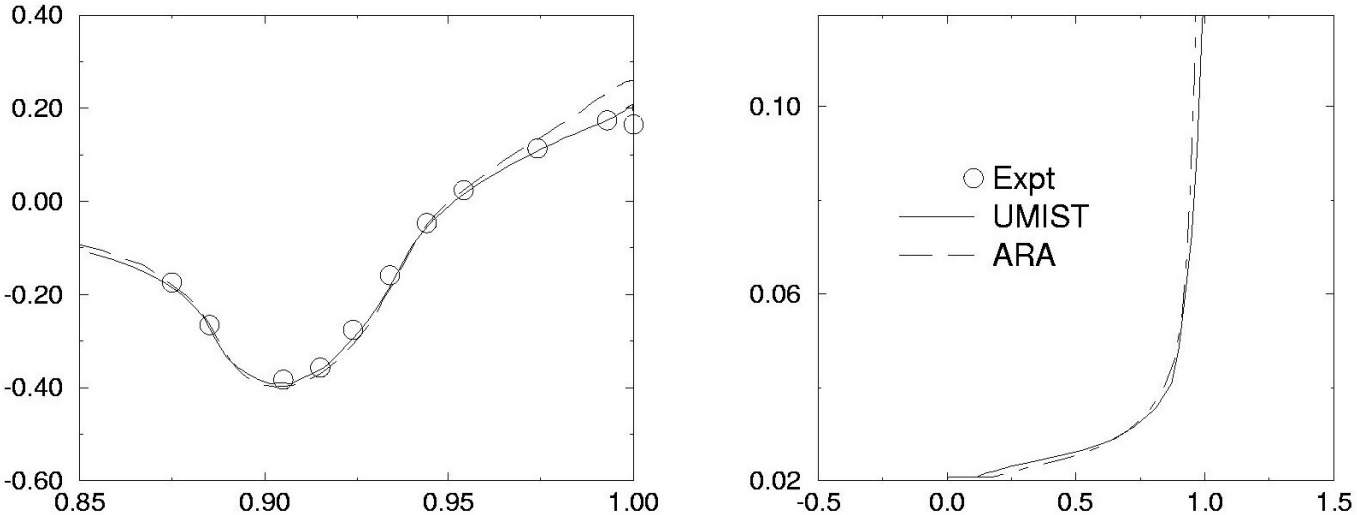


Figure 4. Grid dependency test with standard $k - \varepsilon$ model.



(a) Standard $k - \varepsilon$ for M = 0·94.



(b) Menter SST model for M = 0·60.

Figure 5. Intercode comparison.

https://doi.org/10.1017/S0001924000004942 Published online by Cambridge University Press

zero, regardless of the free-stream conditions. On the far field boundary, away from the surface, the flow was considered to be tangential to the domain. At the jet inflow (inside the nozzle), experimental total pressure and total temperature were specified. The static pressure was extrapolated to the boundary from the interior of the computational domain. Finally, no-slip and adiabatic boundary conditions were imposed on the body surface. The turbulence energy at the inlet, k was taken to be 0·01% of the free-stream mean kinetic energy, and the length-scale variable ε or ω was specified such that $\frac{\mu_t}{\mu} = 1$. These values have little influence on the flow development, and their influence has been extensively studied for a 2D bump (afterbody-sting) test case[5].

5.0 RESULTS AND DISCUSSION

5.1 General features

Calculations were carried out for two free stream Mach numbers of 0·6 and 0·94. The jet total pressure ratio was 4 (defined as the ratio of jet total pressure at inlet to free-stream static pressure) for both cases and hence the flow development inside the convergent-divergent nozzle was essentially ideal (although the small deviation from the nozzle design pressure ratio will induce some small effects (see below)), and also identical for both free stream Mach numbers. However, the flow over the afterbody displayed drastically different features for the two Mach numbers. In both cases, the flow accelerates as the fluid moves towards the aft of the model. For the lower Mach-number case, the flow is well-behaved, and there is no indication that it separates on any of the surfaces. Although none of the calculations in the present work predicted a separation for this lower Mach number, the calculations by Compton[16] using the Baldwin-Lomax [11] turbulence model predicted incipient separation near the exit plane of the afterbody. This is, however, likely to be a defect of this simple algebraic turbulence model.

On the other hand, for the 0·94 Mach number case, the flow accelerates to supersonic speed and this is followed by a strong shock as the flow is blocked by the jet. Due to interaction with the slower moving fluid in the thickened boundary layer, separation occurs at about $X \sim 0{\cdot}90$ and extends well into the plume. This massive separation, most pronounced on the vertical surface, extends to the side walls. A qualitative view of these features is conveyed in Fig. 3 via predicted velocity vectors and surface streamlines. The exit Mach number from the convergent-divergent nozzle is about 1·6, and the jet interacts with the separated flow coming off the afterbody external surface, resulting in a very complex shear layer in the plume region.

5.2 Grid-dependence tests

Figure 4 demonstrates grid independence by way of distributions of static pressure coefficient C_p on the vertical plane and profiles of the axial mean velocity at $X = 1{\cdot}0$, for the higher Mach number. The coarser mesh was generated by removing every alternate grid node in all three coordinate directions, giving a mesh of about 117,000 cells. These computations were performed using the standard $k - \varepsilon$ turbulence model. As seen, the differences between the solutions are modest, including the predicted maximum negative velocity, which is a particularly sensitive feature. All results presented below were obtained with the finer mesh.

5.3 Solution algorithm and intercode comparisons

As mentioned before, one important aspect of the present collaborative research has been to ensure that solutions are free from numerical uncertainties and truly reflect the predictive properties of the turbulence

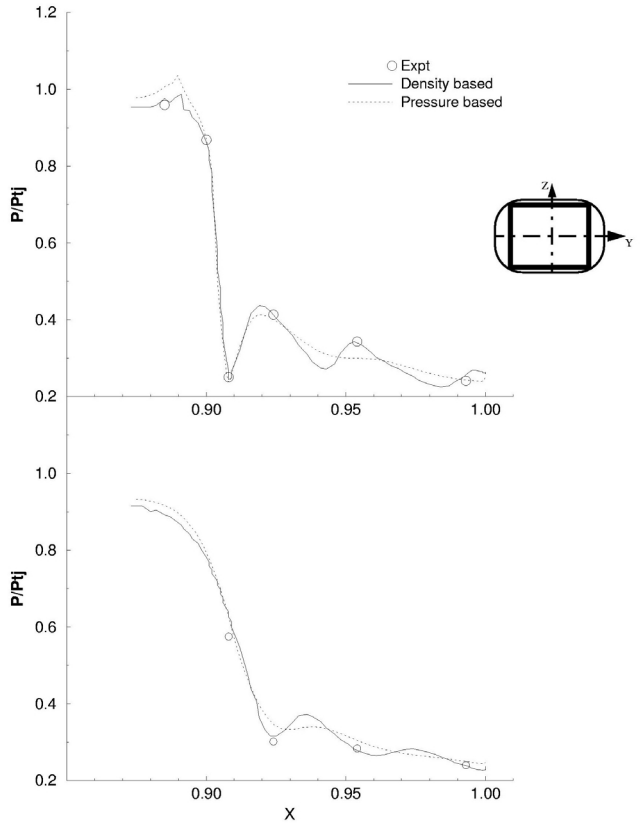


Figure 6(a). Comparison of static pressure ratio along the internal nozzle surface (M = 0·60) (top – along $Y = 0$ surface, bottom – along $Z = 0$ surface).

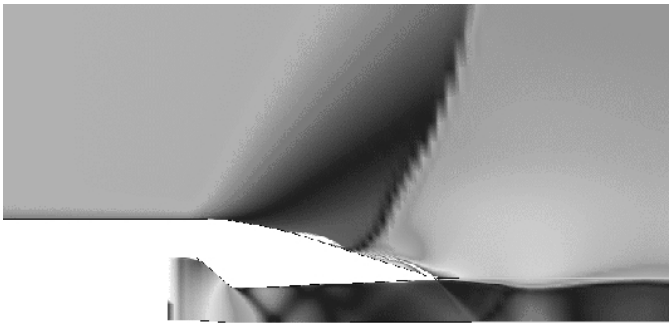


Figure 6(b). Mach contours showing oblique shock inside the nozzle and strong afterbody shock at M = 0·94.

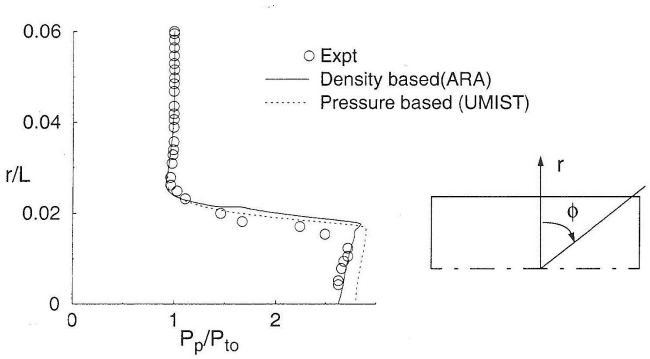


Figure 6(c). Pitot pressure comparison at $X = 1{\cdot}08$, $\phi = 7°$.

https://doi.org/10.1017/S0001924000004942 Published online by Cambridge University Press

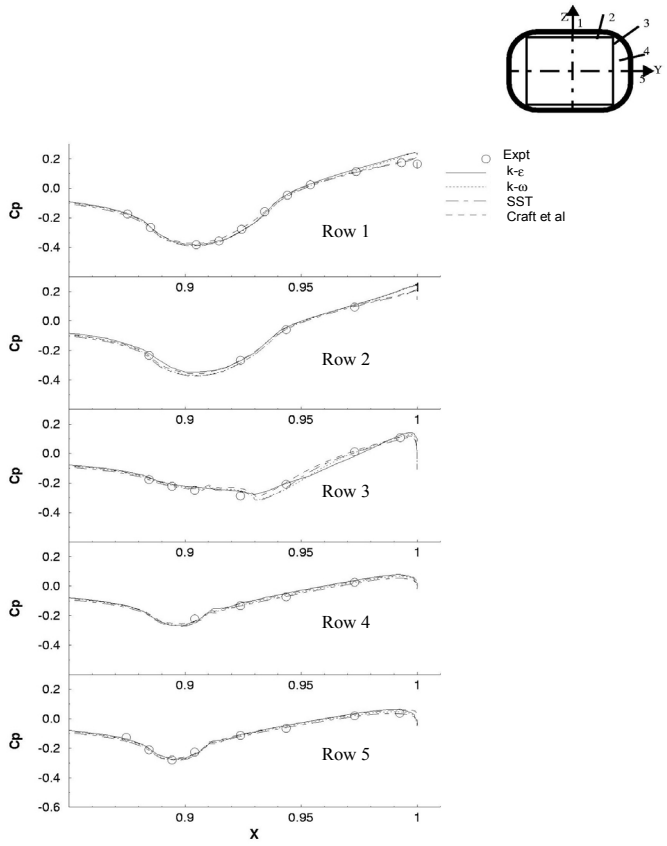


Figure 7. Effect of turbulence model on external surface C_p distribution for M = 0·60

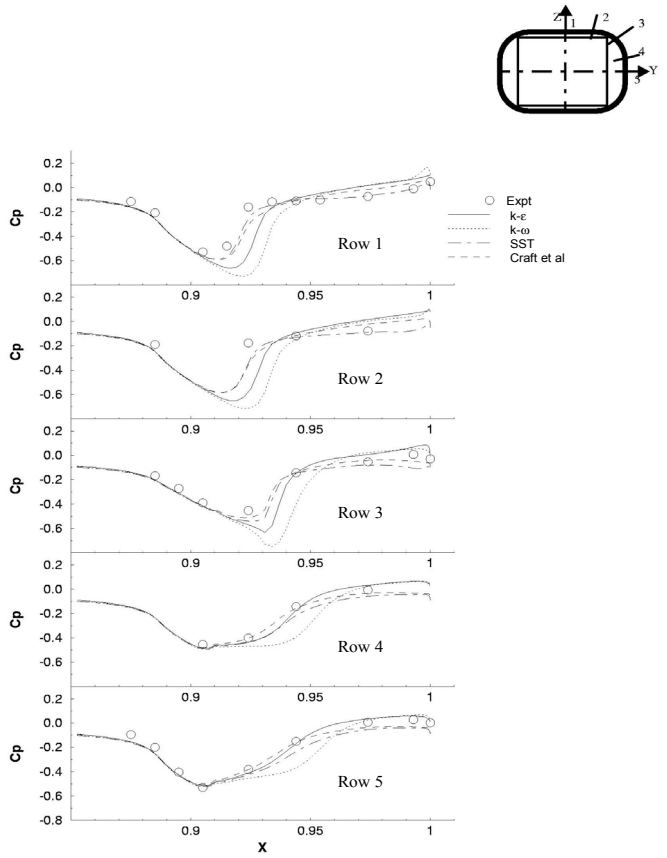


Figure 8. Effect of turbulence model on external surface C_p distribution for M = 0·94

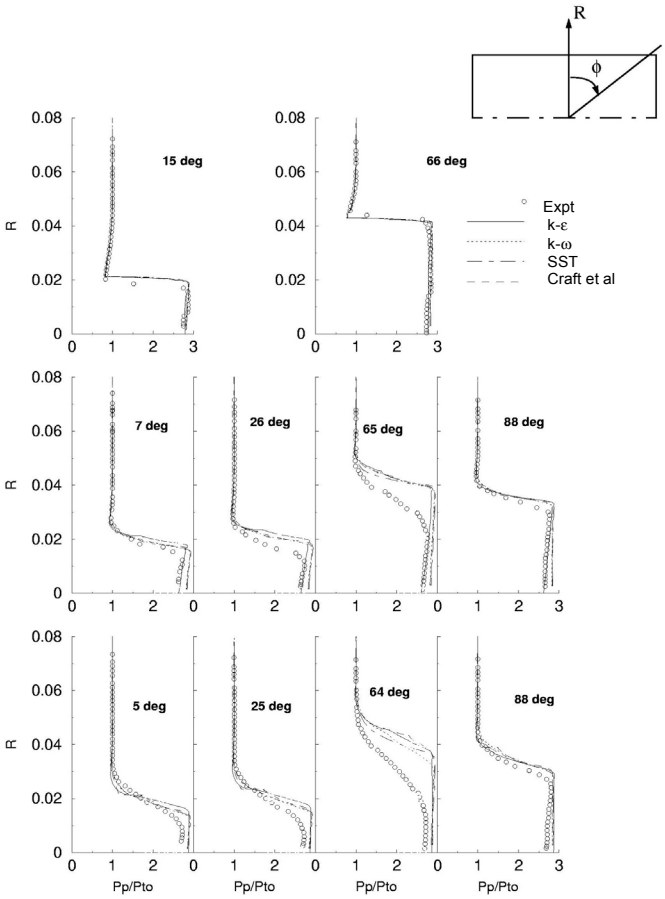


Figure 9. Comparison of pitot pressure in the plume for M = 0·60 (X = 1·0 (top), 1·08 (middle) and 1·16 (bottom)).

model. All partners used their own codes, which mostly employed co-located, cell-centred finite-volume storage. The only exception was ARA who used a cell-vertex scheme, although on the same common mesh. The convection schemes were in all cases second-order accurate TVD approximations. UMIST's and Loughborough's solution algorithms solved for pressure directly, while those of ARA and BAE Systems determined the density from the continuity equation. These same codes had been used in earlier studies[4-6] to predict other flows where they were subjected to detailed scrutiny. Much care was taken in these studies to understand and resolve the differences in the implementation of boundary conditions and models and other subtle issues associated with discretisation of the governing differential equations. This was a lengthy and tedious process, requiring a number of iterations before, finally, all the codes yielded essentially identical results for both linear and non-linear models[4-6]. A similar strategy was also followed in the present investigation.

Intercode comparison for afterbody surface

Comparisons between solutions obtained by Loughborough, UMIST and ARA for C_p along the vertical plane on the afterbody external surface (plane of maximum backflow) and mean velocity U (normalised by the freestream mean velocity) at X = 1·0 for the Mach number 0·94 case are shown in Fig. 5(a). Code-dependence is seen to be minor, giving a good level of confidence in the results; this is in line with previous observations for 2D test cases[4,5]. Similar comparisons for the SST model are presented in Fig. 5(b) for the lower Mach number between solutions by UMIST and ARA. The results are again close.

https://doi.org/10.1017/S0001924000004942 Published online by Cambridge University Press

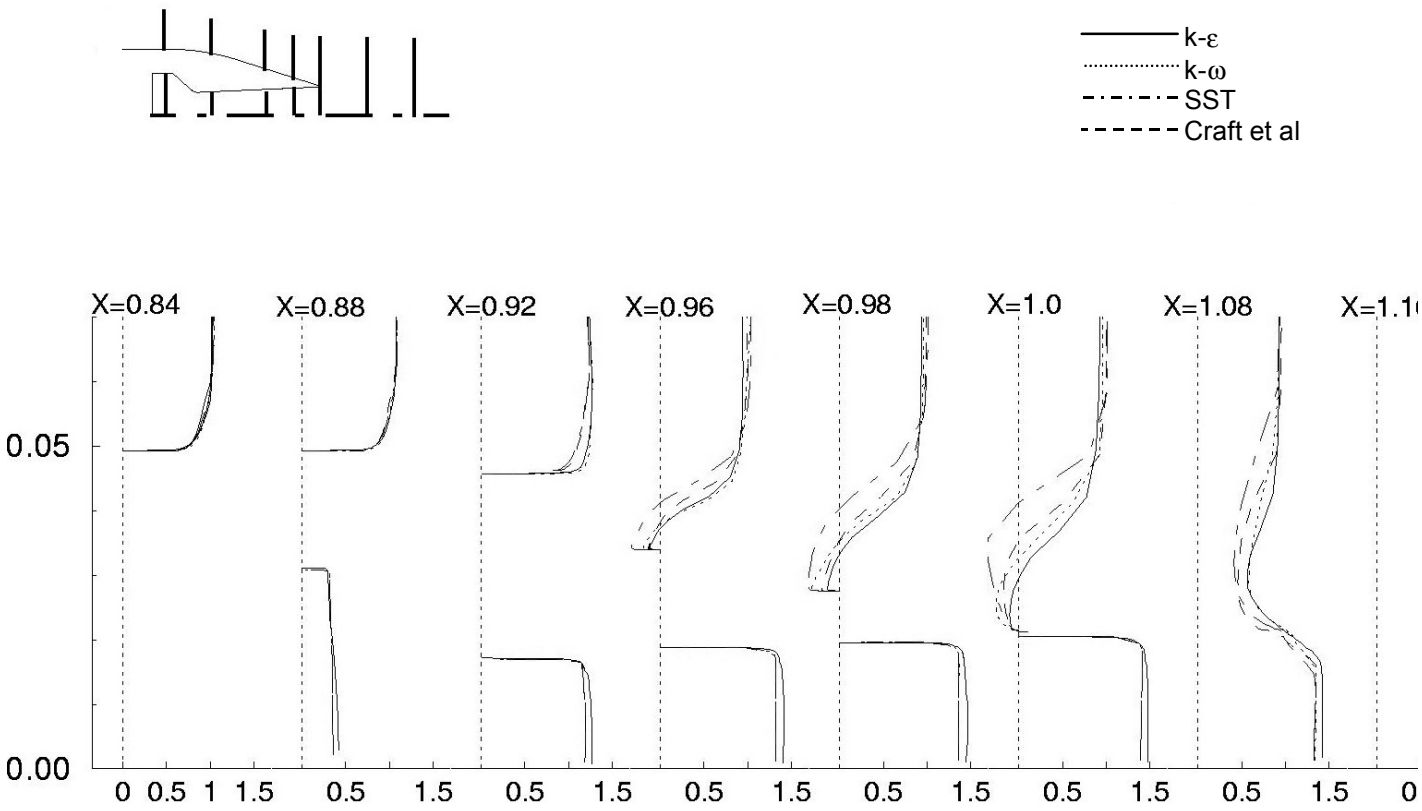


Figure 10(a). Development of streamwise velocity U on the afterbody surface for M = 0·94.

Intercode comparison of pressure inside the nozzle

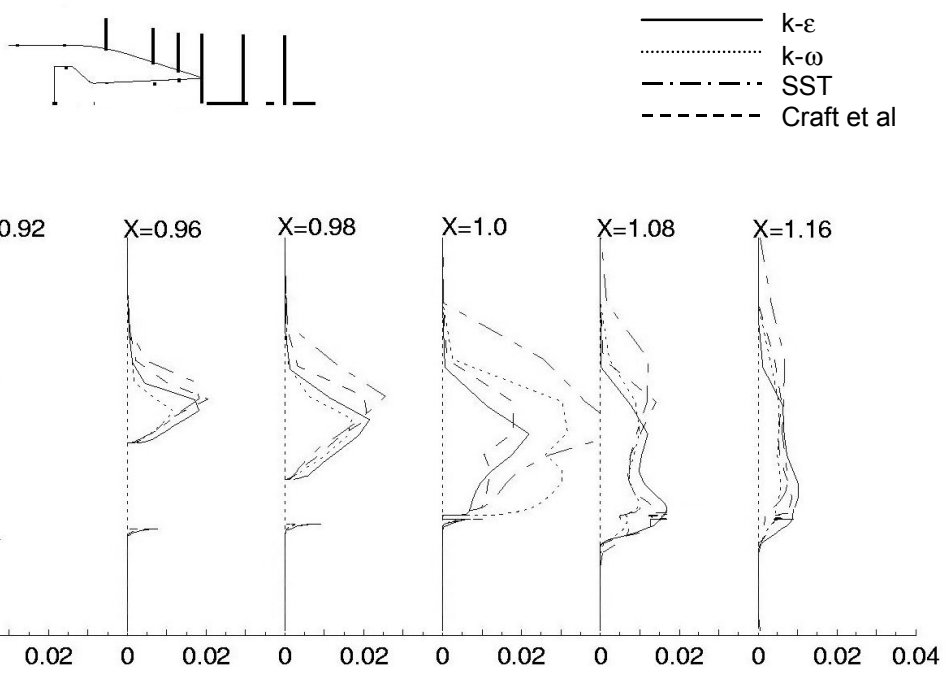
Comparisons were also made for the pressure inside the convergent-divergent nozzle. Although turbulence transport is of no consequence in the nozzle, such comparisons are interesting from a numerical point of view because of the presence of surface-pressure oscillations, signifying shock-reflections due to the slightly off-design running conditions. Figure 6(a) compares the surface static pressure (normalised by the jet total pressure) along the vertical and horizontal planes of the nozzle. In this flow region, solutions for different turbulence models were found to be virtually indistinguishable. The results do, however, show a clear dependence on whether the algorithms are pressure-based or density-based. The smoother pressure curve results from the pressure-based approach. In contrast, the density-based results show distinct spatial oscillations in pressure, identifying shock reflections and being in closer correspondence with measurements. It thus appears that the Mach-dependent density blending (of upwind and central interpolations), which is part of the pressure-based schemes, leads to some shock attenuation, especially if the shocks are weak. Figure 6(b) gives a Mach contour plot arising from the density-based method. Oblique shocks are generated inside the nozzle near the throat, and these are resolved better by the density-based method. Since there is also a small total-pressure loss across the shocks, this better resolution of the inviscid features by the density-based method results in better agreement in respect of the total pressure in the jet core outside the nozzle in the near exit region. This is evident from the results shown in Fig. 6(c). It is important to note here, however, that this algorithm-dependence is confined to weak secondary shocks following multiple reflection and does not impair the examination of turbulence-model performance in the presence of the strong interactions with the boattail shock.

5.4 Effect of turbulence model on afterbody surface pressure

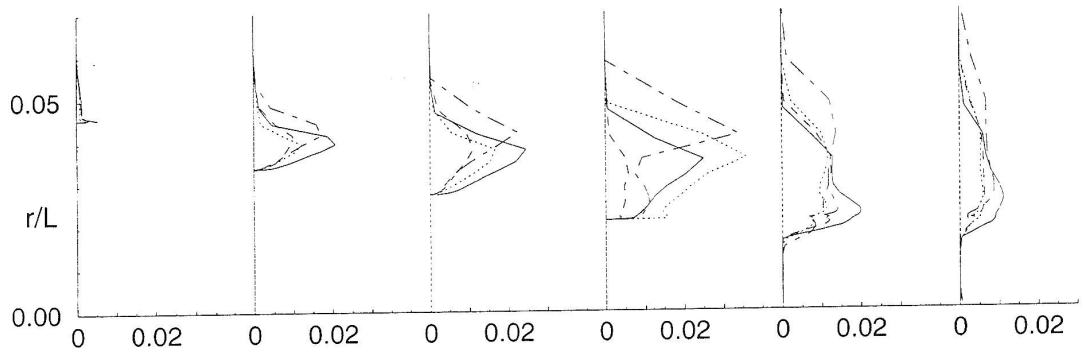
The emphasis of the present paper is on the predictive ability of the different eddy-viscosity turbulence models. For the lower Mach-number case, for which the flow is attached, all models perform well, as can be seen from the C_p comparisons on the afterbody surface in Fig. 7. There is a very slight improvement returned at the far end of the afterbody on Row 1 (X ~ 1·0) by the SST and the NLEVM models. However, the differences are small. It should be mentioned that the somewhat larger differences among the predicted results along Row 3 is due to the fact that this row lies on the sharp edge of the afterbody and hence represents a poor location for interpolated data comparisons.

Analogous plots for the higher Mach number case are shown in Fig. 8. Several interesting features emerge from these results. All the profiles are very close to one another in the accelerating part and agree well with the data. However, the shock position and the separation and recovery behaviour are predicted differently with different turbulence models. The linear $k-\varepsilon$ and $k-\omega$ models give a delayed shock along with a poor recovery up to the plateau in the separation zone after the shock. The $k-\omega$ model shows the largest departure from the experimental data. This is rather unusual and does not concur with our earlier observations for the 2D test cases[4,5,6]. The SST model is seen to yield dramatically improved pressure results. Thus, the shock location and overall pressure recovery are represented to a quality similar to that of the cubic EVM, mainly as a consequence of introducing the shear-stress limiter. The absence of experimental data for velocity prevents a more searching assessment of turbulence-model performance for this flow. It must be said, however, that improved agreement in respect of pressure does not necessarily mean corresponding improvements in other flow quantities. In the earlier investigation of turbulence-model performance for the transonic flow around an axisymmetric bump (afterbody-sting configuration)[6], the SST model was found to return

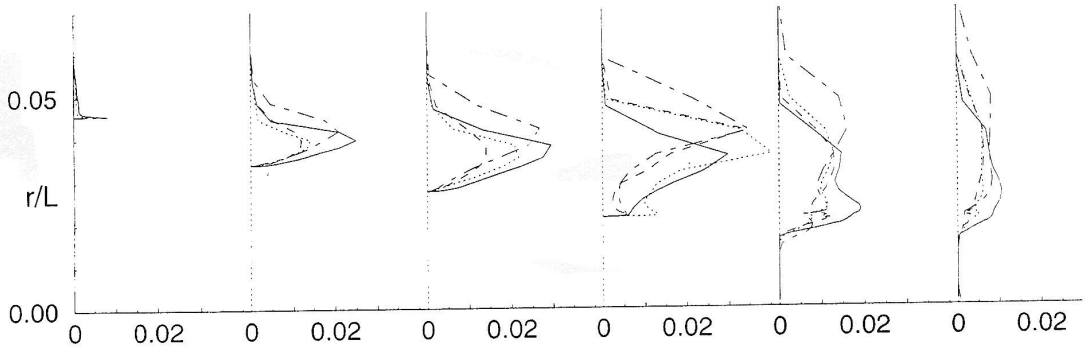
https://doi.org/10.1017/S0001924000004942 Published online by Cambridge University Press



(b) Normal stress $\overline{u}\overline{u}$



(c) Normal stress $\overline{vv}$



(d) Normal stress $\overline{ww}$

Figure 10(b-d). Development of turbulence quantities on the afterbody surface for M = 0·94.

https://doi.org/10.1017/S0001924000004942 Published online by Cambridge University Press

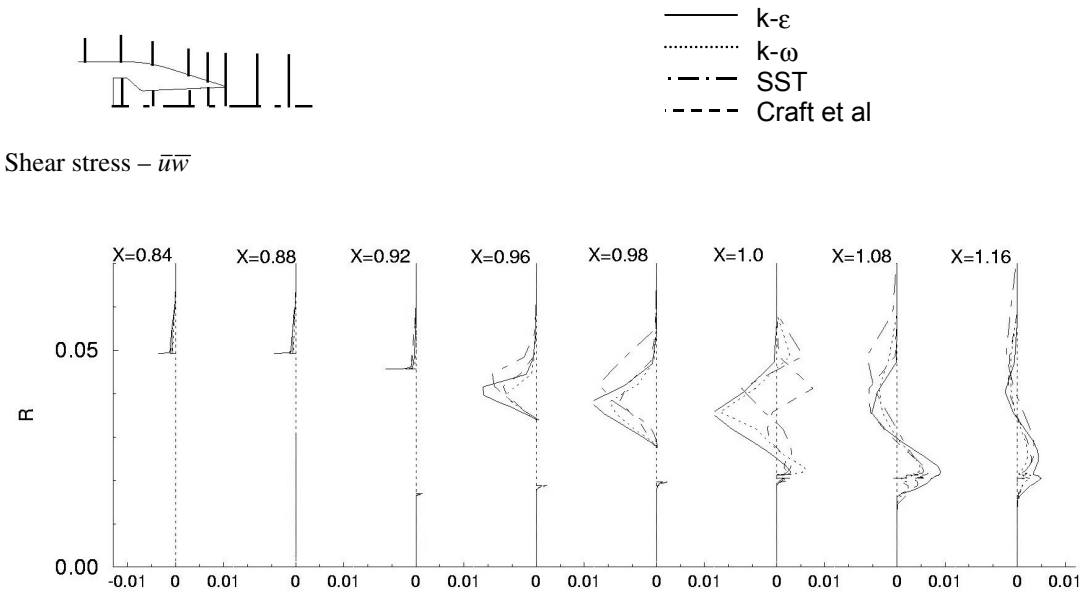


Figure 10(e) Development of shear stress on the afterbody surface for M = 0·94

good results for pressure, but rather poor results for velocity and turbulence quantities. Figure 8 shows that the cubic eddy-viscosity model also gives close to excellent agreement with the experimental data, but reference to[6] shows that this quality of performance also extends to other flow quantities (mean streamwise velocity and turbulent normal stresses).

5.5 Effect of turbulence modelling on plume pressure

Extensive pitot pressure measurements are available for the jet exhaust plume for the free-stream Mach number of 0·60. It is unfortunate that no such measurements were made for the more challenging higher Mach number case. However, some key features of the plume are largely divorced from the afterbody flow and can be investigated profitably for the lower free-stream Mach number.

Comparisons with experimental data are given in Fig. 9 for three streamwise locations: X = 1·0, 1·08 and 1·16. The first set of profiles at ϕ = (0-15°) are near the vertical plane of symmetry, those at ϕ ~ 25° are in a plane that bisects through the top surface of the nozzle, those at 65° are in a plane that intersects the nozzle approximately at its corner and those at 88° are close to the horizontal plane of symmetry.

At the jet exit (X = 1·0), there are hardly any differences between the different models, and the boundary layers are well predicted. These results are distinctly superior to those obtained by ARA in an earlier exercise[2], perhaps due to the fact that, in contrast to[2], the geometry was modelled in full in the present study. The quality of predicted results becomes progressively poorer at downstream locations, however. A common failure of all models, whether implemented in the pressure or density-based schemes, is a poor prediction of the shear layer in the corner region of the domain, especially at around 65°. The spreading rate is severely underpredicted by almost the same amount in all models. While the turbulence models implemented in this study do not include compressibility corrections (specifically for dilatational dissipation), such corrections would only have diminished the predicted spreading rate further. Hence, this is not the origin of disagreement. On the assumption that the experimental data are correct, one possible reason for the poor results is an inadequate resolution of the corner region due to the grid topology used. Specifically, the O-topology and associated distortions do not allow an accurate representation of the viscous terms in the corners.

Clearly, turbulence-model defects are another possible cause. The models used may have failed to predict the cross flow vortices correctly, resulting in the large discrepancy observed in this region. The results do highlight the importance of investigating the flow with differential stress models, but this is only sensible if more experimental data are available. It is appropriate to note here that earlier exercises[2,16] also show qualitatively similar defects in these regions. Furthermore, the use of other grid topologies in the studies referred to did not improve the results, suggesting that it is probably the turbulence model which is the primary culprit.

5.6 Flow development and backflow

To study the flow development on the afterbody outside wall, profiles of mean velocities and Reynolds stresses for both test cases and for both the vertical and horizontal planes are examined in Figs 10 and 11. There are no corresponding experimental data available, however. The most interesting features are revealed in the profiles along the vertical plane for the higher Mach number case, and these are shown in Fig. 10(a-e). The agreement between the different models for the supersonic region within the nozzle is close, confirming the inviscid nature of the flow in this region. The effect of the turbulence model is evident in the external boundary layer, the separation region and the recovering flow thereafter. The SST model gives the largest separation and the highest magnitude of the backflow and thickness of the separation bubble on the vertical plane.

A subset of the velocity and Reynolds-stress profiles given in Fig. 10 are reproduced for X = 1 in Fig. 11. These profiles demonstrate most prominently the features most sensitive to turbulence modelling. Thus, only the cubic model predicts large normal-stress anisotropy, although the accuracy of the anisotropy level cannot be verified. The shear stress profiles display an especially complex pattern for the cubic model, and this is associated with a secondary separation bubble near the vertical plane which this model resolves. The suppression of shear stress by the SST limiter, in comparison with the $k-\omega$ model, is also clearly recognised in the plot for $\overline{uw}$.

More quantitative information about the strength of the backflow, in terms of maximum reverse velocity (U_{max}) and separation-bubble height (δ), is given in Fig. 12. The maximum backflow is normalised by the freestream velocity and separation height by the model length L.

https://doi.org/10.1017/S0001924000004942 Published online by Cambridge University Press

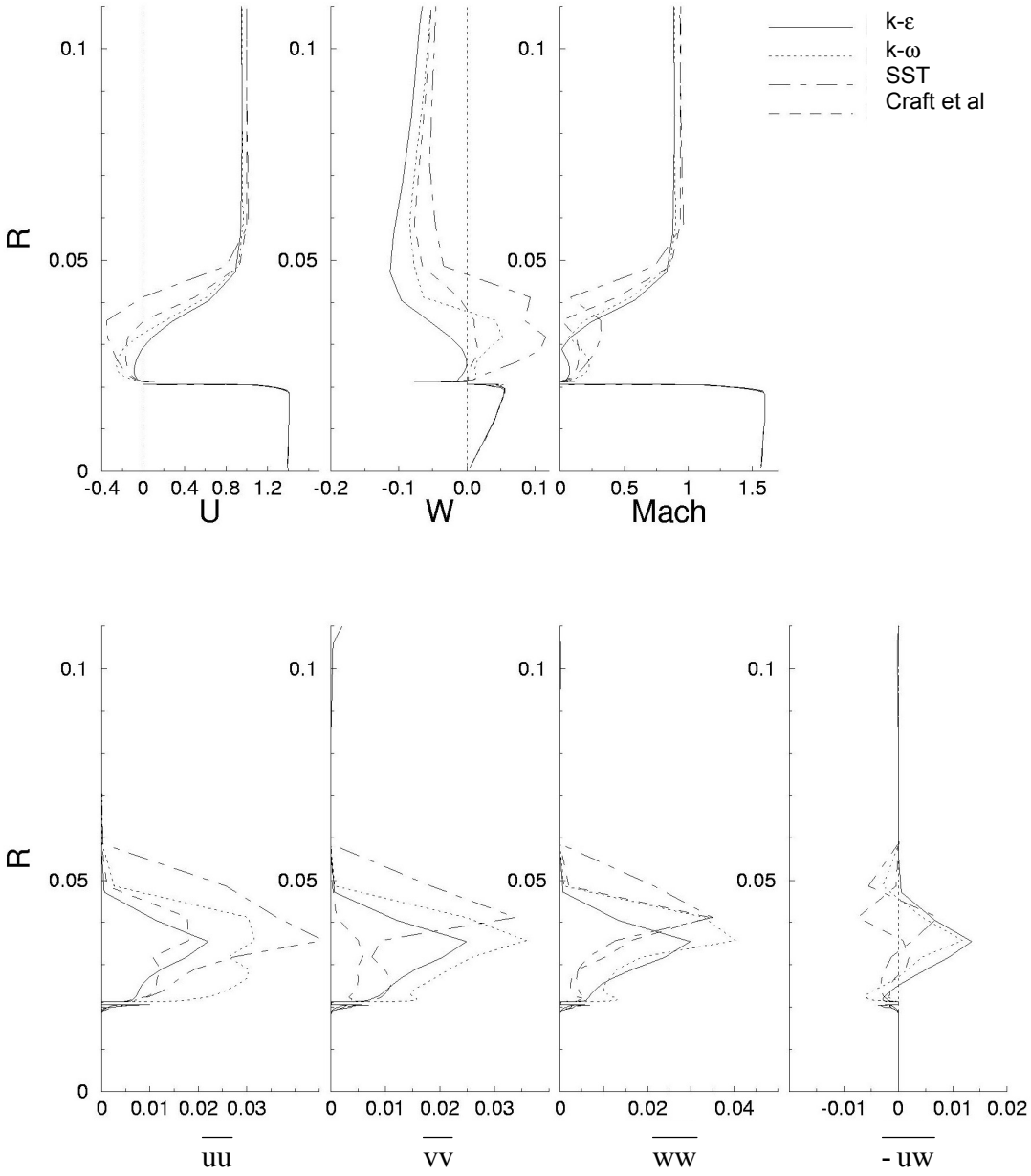


Figure 11. Mean and turbulent quantities at $X = 1{\cdot}0$ in vertical plane for M = 0·94.

The cubic model shows a weaker backflow than the SST or $k - \omega$ model. On the basis of observations in 2D test cases, it is tempting to conclude that the SST model gives excessive separation and this is implied by Figs 11 and 12. However, as observed earlier, it is dangerous to extrapolate from 2D to 3D flows. The only true test would be based on experimental data of both mean and turbulence quantities in the separation zone at M = 0·94. The present investigation shows there is an urgent need for such data.

6. CONCLUSIONS

A numerical investigation was conducted to assess the predictive ability of various turbulence models for predicting shock/boundary-layer interaction on a non-axisymmetric jet/afterbody configuration. One outstanding feature of this study was that the results presented are an outcome of a collaborative effort in which uncertainties associated with code-dependence, solution algorithms, grids, boundary conditions and model implementation have been carefully evaluated and addressed. This process was tedious and lengthy, but was essential for confidence in the conclusions drawn on the relative model performance.

One conclusion emerging from the work is that, as long as the flow remains attached, the performance of the eddy-viscosity models examined is adequate and fairly uniform, at least for the flow variables considered in this study. Hence such models may be used for design purposes with a good level of confidence. The situation changes drastically with the onset of separation due to strong interaction at high Mach numbers when the models return different sensitivity levels to the flow features. The standard $k - \varepsilon$ model retards the shock with consequent high values of pressure in the post-shock region. The $k - \omega$ model yields an even greater shock retardation. Results are drastically improved with Menter's SST model, as far as C_p is concerned. The location of the shock and the subsequent

https://doi.org/10.1017/S0001924000004942 Published online by Cambridge University Press

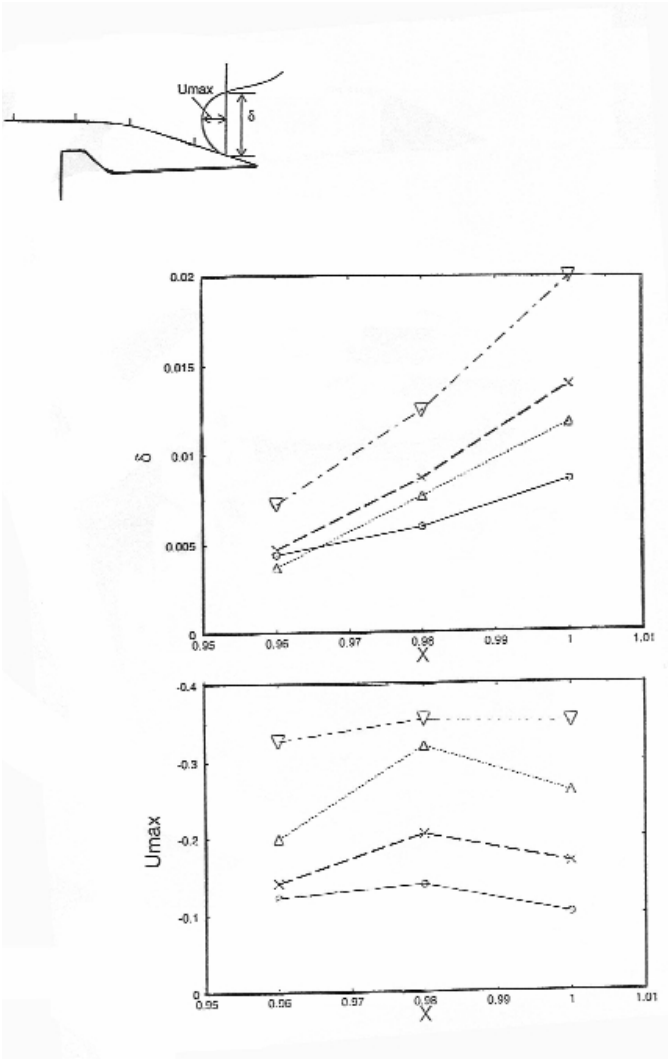


Figure 12. Recirculation height in vertical plane and maximum backflow for M = 0·94. (*SST* (∇), Craft *et al* (X), $k-\omega$(Δ), $k-\varepsilon$(O))

recovery agree well with the experimental data. However, earlier results for other configurations suggest that this very positive observation may not extrapolate to field quantities. The non-linear eddy-viscosity model gives, overall, the best prediction. Although no statements can here be made on boundary-layer profiles, experience in other shock/bondary-layer flows suggests that this model also returns a good representation of the velocity profiles. This is the only model which produces significant anisotropy of normal stresses.

Another interesting observation is the algorithm-dependence in resolving the reflected shock system inside the nozzle. For identical grids and boundary conditions, the density-based codes are found to resolve the pressure fluctuations associated with multiple shock reflection more accurately than a pressure-based code. The flow inside the nozzle is essentially inviscid, and no effect of turbulence modelling can be observed here.

The study also considered the plume structure for the unseparated lower Mach number case. Agreement is good in the symmetry planes but not in the corner regions.

Finally, the study highlighted the urgent need to carry out more experiments to obtain reliable velocity and turbulence data, particularly in the separation zone at higher free-stream Mach numbers.

ACKNOWLEDGEMENTS

The work presented here would not have been possible without the active support of a number of colleagues who have contributed to this work within the VOTMATA consortium. We are grateful for their permission to use their CFD predictions in the present paper. Special thanks go to Dr Alan Gould and Dr Stephen Moir (BAE Systems – SRC), Dr Nick May and Dr Moira Maina (Aircraft Research Association), Professor Tony Hutton (QinetiQ) and Mr John Coupland and Dr Nadji Chioukh (Rolls-Royce plc). The financial suipport provided by the UK Engineering and Physical Sciences Research Council (through EPSRC Grant No. GL/L/58804), BAE SYSTEMS, RR and DERA is gratefully acknowledged.

REFERENCES

1. AGARD 1986, Aerodynamics of 3D aircraft afterbodies, AGARD Advisory Report, (226).
2. AGARD 1995, Aerodynamics of 3D aircraft afterbodies, AGARD Advisory Report, (318).
3. PUTNAM, L.E. and MERCER, C.E. Pitot-pressure measurements in flow fields behind a rectangular nozzle with exhaust jet for free-stream Mach numbers of 0·0, 0·60 and 0·94, 1986, NASA TM-88990.
4. APSLEY, D.D. and LESCHZINER, M.A, Advanced turbulence modelling of separated flow in a diffuser, 1999, *Flow Turbulence and Combustion*, **63**, pp 81-112.
5. APSLEY, D.D. and LESCHZINER, M.A. Investigation of advanced turbulence models for the flow in a generic wing-body junction, 2001, *Flow Turbulence and Combustion* (in press).
6. HASAN, R.G.M. and MCGUIRK, J.J. Assessment of turbulence model performance for transonic flow over an axisymmetric bump, *Aeronaut J*, 2001, **105**, (1043), pp 17-31.
7. CARSON, G.T. and LEE, E.E. Experimental and analytical investigation of axisymmetric supersonic cruise nozzle geometry at Mach numbers from 0·60 to 1·30, 1981, NASA TP 1953.
8. REUBUSH, D.E. Effects of finess and closure ratios on boattail drag on circular-arc-afterbody models with jet exhaust at Mach numbers up to 1·3, 1973, NASA TN D-7168.
9. REUBUSH, D.E. The effect of Reynolds number on boattail drag, AIAA Paper 75-63, AIAA 13th Aerospace Sciences Meeting, Reno, 1975.
10. BACHALO, W.D. and JOHNSON, D.A. Transonic turbulent boundary-layer separation generated on an axisymmetric flow model, 1986, *AIAA J*, **24**, pp 437-443.
11. BALDWIN, B.S. and LOMAX, H. Thin layer approximation and algebraic model for separated turbulent flows, 1978, AIAA Paper 78-257.
12. GOLDBERG, U.C., Separated flow treatment with a new turbulence model, *AIAA J*, 1986, **24**, pp 1711-1713.
13. PEACE, A.J., Turbulent flow predictions for afterbody/nozzle geometries including base effects, *J Prop and Power*, 1991, **7,** (3), pp 396-403.
14. NEWBOLD, C.M. Solution to the Navier-Stokes equations for turbulent transonic flows over axisymmetric afterbodies, 1990, Report ARA TR 90-16.
15. CARLSON, J.R., PAO, S.P., ABDOL-HAMID, K.S. and JONES, W.T. Aerodynamic performance predictions of single and twin jet afterbodies, AIAA Paper 95-2622, 1995.
16. COMPTON, W.B. Comparison of turbulence models for nozzle-afterbody flows with propulsive jets, NASA TP-3592, 1996.
17. CARLSON, J.R., High Reynolds number analysis of flat plate and separated afterbody flow using non-linear turbulence models, AIAA Paper 95-2622 1996,.
18. LOYAU, H., BATTEN, P. and LESCHZINER, M.A. Modelling shock/boundary-layer interaction with nonlinear eddy viscosity closures, *Flow Turbulence and Combustion,*1998, **60**, pp 257-282.
19. BATTEN, P., CLARKE, N., LAMBERT, C. and CAUSON, D.M., 1997, On the choice of wave speeds for the HLLC Riemann solver, SIAM *J Sci and Stat Comp,* 1997, **18,** (6), pp. 1553-1570.
20. LESCHZINER, M.A., BATTEN, P. and CRAFT, T.J. Reynolds-stress modelling of transonic afterbody flows, *Aeronaut J*, 2001, **105**, (1048), pp 297-306.
21. BARAKOS, G. and DRIKAKIS, D. 2000, Investigation of non-linear eddy-viscosity models in shock/boundary-layer interaction, *AIAA J*, **38**, pp. 461-469.
22. BERRIER, B.L. A selection of experimental test cases for the validation of CFD codes, Technical report, 1988, AGARD AR-303, **2**.

https://doi.org/10.1017/S0001924000004942 Published online by Cambridge University Press

23. MENTER, F.R., Two-equation eddy-viscosity models for transonic flows, *AIAA J*, 1994, **32**, pp 1598-1605.
24. COMPTON, W.B., ABDOL-HAMID, K.S. and ABEYOUNIS, W.K. Comparison of algebraic turbulence models for afterbody flows with jet exhaust, 1992, *AIAA J*, **30**, pp 2716-2722.
25. COMPTON, W.B., ABDOL-HAMID, K.S. Navier-Stokes simulations of transonic afterbody flows with jet exhaust, 1990, AIAA Paper 90-3057.
26. JONES, W.P. and LAUNDER, B. E. The prediction of laminarization with a two-equation model of turbulence, 1972, *Int J Heat and Mass Transfer*, **15**, pp 301-314.
27. WILCOX, D. C., Reassessment of the scale-determining equation for advanced turbulence models, *AIAA J*, 1988, **26**, pp 1299-1310.
28. CRAFT, T. J., LAUNDER, B.E. and SUGA, K. Prediction of turbulent transitional phenomena with a non-linear eddy-viscosity model, 1997, *Int J Heat Fluid Flow*, **18**, pp 15-28.
29. APSLEY, D. D. and LESCHZINER, M.A. A new low-Re non-linear two-equation turbulence model for complex flows, *Int J Heat Fluid Flow, 1998,* **19**, pp 209-222.

https://doi.org/10.1017/S0001924000004942 Published online by Cambridge University Press